

# Mechanics of curved crease origami: 1DoF mechanisms, distributed actuation by spontaneous curvature, and cross-talk between multiple folds

Antonio DeSimone<sup>a,b,\*</sup>, Luciano Teresi<sup>c</sup>

<sup>a</sup>The BioRobotics Institute, Scuola Superiore Sant'Anna, viale Rinaldo Piaggio 34, 56025 Pontedera, Italy

<sup>b</sup>SISSA–International School for Advanced Studies, via Bonomea 265, 34136 Trieste, Italy

<sup>c</sup>Department of Industrial Engineering–Università Roma TRE, 00146 Roma, Italy

---

## Abstract

Origami morphing, obtained with patches of piecewise smooth isometries separated by straight fold lines, is an exquisite art that has already received considerable attention in the mathematics and mechanics literature. Curved fold lines, leading to curved creases and curved pleated structures, introduce the additional complexity of mechanical coupling between the folds. This coupling can be exploited to obtain morphing structures with more robust folding pathways. We discuss one-degree-of-freedom mechanisms and folds actuated by spontaneous curvature (as in the case of hygromorphic multilayered composites), comparing the purely geometric approach to two approaches based on the mechanics of active shells and of active three-dimensional solids. Moreover, we discuss the cooperativity of multiple folds and demonstrate the energetic advantage of synchronous folding over sequential folding.

*Keywords:* Origami, curved creases, deployable structures, Gaussian morphing, active shells, soft robotics

---

## Contents

<b>1</b>	<b>Introduction</b>	<b>2</b>
<b>2</b>	<b>Two motivating examples: results using geometric models, active shells, and 3D active solids</b>	<b>2</b>
2.1	Geometric approach: actuation by folding angle . . . . .	3
2.2	Mechanical modeling . . . . .	6
2.2.1	Approach by active shell models: actuation by target curvature . . . . .	8
2.2.2	Approach by 3D active elasticity models: actuation by target metric . . . . .	8
<b>3</b>	<b>Role of geometry of a single fold-line: circular arcs vs trigonometric functions</b>	<b>9</b>
<b>4</b>	<b>Interaction between folds: synchronous vs sequential folding in an array of 4 identical circular folds</b>	<b>9</b>

---

\*Corresponding author.

*Email address:* a.desimone@santannapisa.it, desimone@sissa.it (Antonio DeSimone)

<b>5 Interaction between folds: fold pairs of circular and trigonometric arcs with different radii or heights</b>	<b>11</b>
5.1 Mechanics modeling	12
5.1.1 The 3D model	12
5.1.2 The Shell model	14
5.2 Geometries	15

## 1. Introduction

Origami morphing, typically obtained with patches of piecewise smooth isometries separated by straight fold lines, is an exquisite art that has already received considerable attention in the mathematics and mechanics literature.

The variant in which the fold lines are not straight is particularly intriguing. Besides the interest acquired in the fields of art, design, manufacturing, and architecture, mastering curved pleated structures requires answering to a number of fundamental questions. From the point of view of mechanics, curvature of the fold-lines introduces the opportunities and challenges due to the fact that the folds become mechanically coupled. This can be exploited to engineer complex deployable structures whose folding and unfolding can nevertheless be controlled robustly (i.e., in a foolproof fashion) through the actuation of few degrees of freedom (DoFs): we discuss here an important example of a 1 DoF mechanism and of its variant obtained by diffuse actuation via spontaneous curvature. In addition, coupling between the folds can be exploited to engineer morphing structures exhibiting multi-stability and preferred folding pathways: as an example, we discuss synchronous versus sequential folding for hyper-extensible tubular structures.

The differential geometry of origami obtained by folding along curves, rather than straight lines, has also been investigated by the mathematical community. While the local geometry of folding along a single curve is well understood (see Section 2.1 and Appendix 1), unraveling the global consequences of nontrivial patterns of fold lines (such as, for example, the case of an annulus with multiple concentric circular fold lines, see Alese (2022)) poses challenges that are still unmet. The key problem here is to understand the cross-talk between the various prescribed fold-lines. This question of how a curved fold propagates to the next prescribed fold line is very closely related to the one of how distinct neighboring folds interact mechanically, which is the central question motivating our study.

In this paper, we focus on the interplay between the geometry and the mechanics of curved folds, and on the issue of cooperative vs antagonistic interactions among multiple folds. Our approach has been inspired by the large existing literature, from which we single out the following contributions: Fuchs and Tabachnikov (2006), Tachi (2011), Demaine et al. (2018), Jiang et al. (2019), Alese (2022), Gao et al. (2020), Tahouni et al. (2020), Liu and James (2024), Feng et al. (2024).

## 2. Two motivating examples: results using geometric models, active shells, and 3D active solids

We set the stage for our discussion of curved-crease origami by first considering two key examples. The first is the analysis of a single fold line shaped as a circular arc and actuated by the folding angle in the center, see Section 2.1. Here, the results are the proof that this is a 1 DoF mechanism and that there is a maximal extent of the fold line before the (local) construction breaks down because of overlapping of the two folds.

The second motivating example is the analysis of the tapering of two curved pleats separated by a single fold line shaped as a circular arc and actuated by spontaneous (or target) curvature

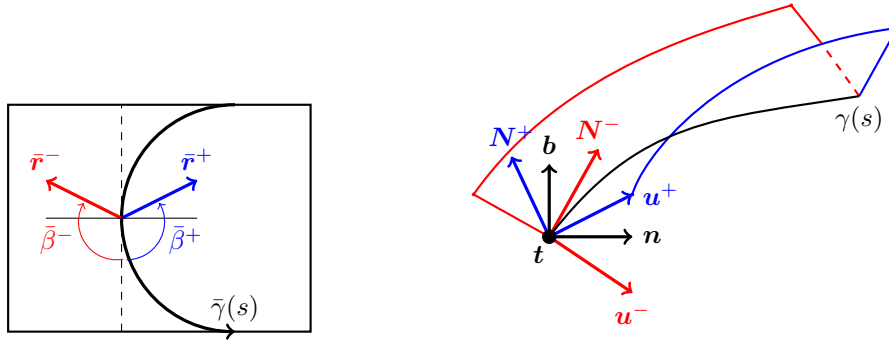


Figure 1: Local geometry of folding along a single curve. Left. Flat state before folding, with the 2D fold line  $\bar{\gamma}$ . Right. Deformed state reached after the folding, with the 3D crease  $\gamma$ . Notation and terminology. Frenet frame:  $t, n, b$ . Darboux frame:  $t, u^\pm, N^\pm$ .

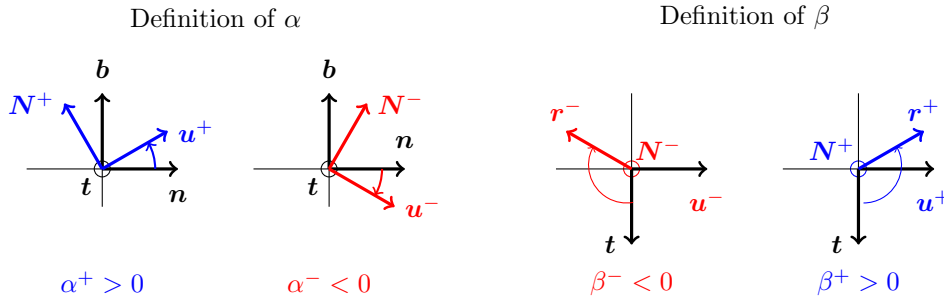


Figure 2: Definition of the angles  $\alpha$  and  $\beta$ .

of the pleats, see Section 2.2. By ‘tapering’ we mean the increase of the visible curvature of the pleats towards the target value as we move away from the curved crease that joins them. Here, the result is an explanation of the tapered shape predicted by mechanics and observed experimentally in synthetic hygromorphic structures.

The second example, where we consider a mechanism of diffuse actuation throughout the surface of the folding structure should be contrasted against the first one, where actuation is concentrated, through the control of the folding angle at a single point along the fold line.

### 2.1. Geometric approach: actuation by folding angle

In this section, we present the theory for the local geometry of folding along a single curve, and discuss some of its applications. We start by introducing the notation to describe the geometry of the sheet and of the curved fold-line, both in the flat state before folding, and in the deformed state reached after the folding has taken place, see Fig. 1, left and right panels, respectively.

We call *fold line* the planar curve  $S \mapsto \bar{\gamma}(S)$  where  $S$  is the arc length. We call *ridge* or *crease* its image after deployment by folding, which is a spatial curve  $s \mapsto \gamma(s)$ , where  $s$  is the arc-length. Since the deployment map is a (continuous, piece-wise) isometry, then the map  $s = s(S)$  is the identity and  $s$  is arc-length on both  $\bar{\gamma}$  and  $\gamma$ . The ridge  $\gamma$  separates two regions of a continuous surface with respective normals  $N^+, N^-$ , typically shaped as developable strips, that we call *folds* or *pleats*.

We denote the Frenet frame along  $\gamma$  with  $\{\mathbf{t}, \mathbf{n}, \mathbf{b}\}$  and the Darboux frames with  $\{\mathbf{t}, \mathbf{u}^\pm, \mathbf{N}^\pm\}$ . Let  $\alpha^\pm$  be the angle that brings  $\mathbf{n}$  onto  $\mathbf{u}^\pm$ , see Fig. 2; we have then

$$\mathbf{u}^\pm = \cos \alpha^\pm \mathbf{n} + \sin \alpha^\pm \mathbf{b}. \quad (1)$$

The two surfaces joined by the ridge  $\gamma$  may be developable. In this case, we write them as

$$\mathbf{x}(s, v) = \gamma(s) + v\mathbf{r}^\pm(s), \quad v \in [0, \text{width}^\pm > 0] \quad (2)$$

where the unit vector  $\mathbf{r}^+(s)$  (resp.,  $\mathbf{r}^-(s)$ ) gives the direction of the ruling at  $\gamma(s)$  on the positive (resp., negative) side of the surface. Denoting by  $\beta^\pm(s)$  the angle that brings  $\mathbf{t}(s)$  onto  $\mathbf{r}^\pm(s)$ , the components of  $\mathbf{r}^\pm(s)$  in the Darboux frames  $\{\mathbf{t}, \mathbf{u}^\pm, \mathbf{N}^\pm\}$  are  $(\cos \beta^\pm, \sin \beta^\pm, 0)$  and hence

$$\mathbf{r}^\pm(s) = \cos \beta^\pm \mathbf{t} + \sin \beta^\pm (\cos \alpha^\pm \mathbf{n} + \sin \alpha^\pm \mathbf{b}). \quad (3)$$

We recall the Frenet formulas for the ridge  $\gamma$  seen as a space curve

$$\frac{d\mathbf{t}}{ds} = \kappa \mathbf{n}, \quad \frac{d\mathbf{n}}{ds} = -\kappa \mathbf{t} + \tau \mathbf{b}, \quad \frac{d\mathbf{b}}{ds} = -\tau \mathbf{n} \quad (4)$$

where  $\kappa$  is the curvature and  $\tau$  is the torsion, and the Darboux formulas for  $\gamma$  seen as a curve traced on either of the two surfaces with normal  $\mathbf{N}^\pm$  (the pleats separated by  $\gamma$ )

$$\frac{d\mathbf{t}}{ds} = \kappa_g^\pm \mathbf{u}^\pm + \kappa_N^\pm \mathbf{N}^\pm, \quad \frac{d\mathbf{u}^\pm}{ds} = -\kappa_g^\pm \mathbf{t} + \tau_r^\pm \mathbf{N}^\pm, \quad \frac{d\mathbf{N}^\pm}{ds} = -\kappa_N^\pm \mathbf{t} - \tau_r^\pm \mathbf{u}^\pm \quad (5)$$

where  $\kappa_g^\pm$ ,  $\kappa_N^\pm$ , and  $\tau_r^\pm$  are geodesic curvature, normal curvature and relative torsion of  $\gamma$  with respect to the surface with normal  $\mathbf{N}^\pm$ , see do Carmo (1976). For the planar curve  $\bar{\gamma}$  (the fold line, namely, the inverse image of the crease  $\gamma$  before folding) formulas (4) and (5) become

$$\frac{d\bar{\mathbf{t}}}{ds} = \bar{\kappa} \bar{\mathbf{u}}, \quad \frac{d\bar{\mathbf{u}}}{ds} = -\bar{\kappa} \bar{\mathbf{t}}, \quad \frac{d\bar{\mathbf{N}}}{ds} = 0 \quad (6)$$

where  $\bar{\mathbf{N}}$  is the normal to the plane containing the pleats before folding, and  $\bar{\mathbf{u}} = \bar{\mathbf{n}}$  is the normal to  $\bar{\gamma}$ .

Folding is realized by a continuous piece-wise isometry. This puts stringent constraints on the admissible folded geometries (kinematic compatibility conditions, akin to the Hadamard jump conditions on the gradients of a continuous piecewise affine map). Since isometries preserve distances, angles, and geodesic curvature, we have that

$$\beta^\pm = \bar{\beta}^\pm, \quad \kappa_g^\pm = \bar{\kappa}. \quad (7)$$

Then, continuity of the folding map together with standard results of differential geometry imply

$$\kappa_N^- = \pm \kappa_N^+ \quad (8)$$

and

$$\alpha^- = -\alpha, \quad \text{where } \alpha := \alpha^+, \quad (9)$$

so that the dihedral angle of the folded ridge, which we call the *folding angle*  $\theta$ , is bisected by the normal  $\mathbf{n}$  and can be written as

$$\theta := \pi - (\alpha^+ - \alpha^-) = \pi - 2\alpha. \quad (10)$$

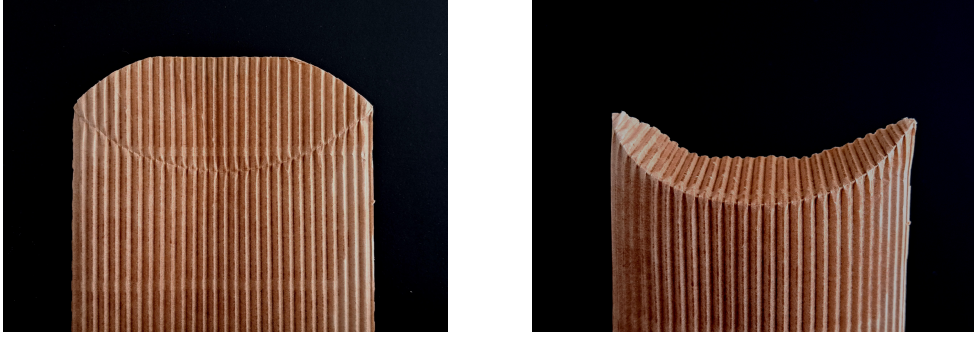


Figure 3: Example of circular arc fold line with corrugated cardboard. Flat configuration (left) and curved one (right).

We notice that  $\alpha = \pm\pi/2$  corresponds to  $\theta = 0, 2\pi$ , respectively, and that

$$\kappa = \frac{\bar{\kappa}}{\cos \alpha} \geq \bar{\kappa}. \quad (11)$$

Using (9), and since  $\tau_r/\kappa_N = \cot \beta$ , it follows that (see do Carmo (1976); Fuchs and Tabachnikov (2006) for details):

$$\cot \beta^\pm = \frac{\tau + (\alpha^\pm)'}{\kappa_g^\pm \tan \alpha^\pm} = \pm \frac{\tau \pm (\alpha)'}{\bar{\kappa} \tan \alpha}$$

and, by adding and subtracting, we deduce that

$$\cot \beta^+ + \cot \beta^- = \frac{2}{\bar{\kappa}} \frac{\alpha'}{\tan \alpha}, \quad (12)$$

$$\cot \beta^+ - \cot \beta^- = \frac{2}{\bar{\kappa}} \frac{\tau}{\tan \alpha}. \quad (13)$$

Consider now the special case of a piecewise isometry in which the rulings are collinear in the flat state ( $\bar{\beta}^+ - \bar{\beta}^- = \pi$ ). An example of a physical system realizing this condition is given by foldable containers made of corrugated cardboard, **see Figure 3**. Since angles on a surface are preserved by isometries, we also have  $\beta^\pm = \bar{\beta}^\pm$  and it follows from (12),(13) that  $\tau = 0$  (hence the folded ridge is always a planar curve!) and

$$\frac{\alpha'}{\tan \alpha} = \frac{\bar{\kappa}}{\tan \beta} = \frac{|\beta'|}{\tan \beta}, \quad (14)$$

where  $\beta := \bar{\beta}^+$ . ODE (14) is easily integrated and the profile  $\alpha(s)$  is uniquely determined by the initial condition  $\alpha(0) = \alpha_0$ . This single scalar parameter, that controls the folding angle  $\theta = \pi - 2\alpha$  at one point ( $s = 0$ ) of the ridge, uniquely determines the curvature  $\kappa$  of the planar ridge  $\gamma$  via (11) ( $\kappa = \bar{\kappa}/\cos \alpha$ ). The curve  $\gamma$  is then recovered (modulo rigid motions) from the knowledge of  $\kappa$  and  $\tau = 0$ . The whole pleated structure (one fold) is then reconstructed from (2). In this way a one-parameter family of curved creases is obtained, parameterized by the angle  $\alpha_0$ , which can be continuously unfolded to the flat state (that is, a one-DoF mechanism).

The existence of solutions of ODE (14) in a neighborhood of  $s = 0$  guarantees that the sheet can be folded locally along the prescribed fold line  $\bar{\gamma}$ . The next question is the maximal interval of existence over which this solution can be continued, i.e. the maximal arc length distance  $s^*$  over which the sheet can be folded along  $\bar{\gamma}$ . To explore this question in a concrete example, we

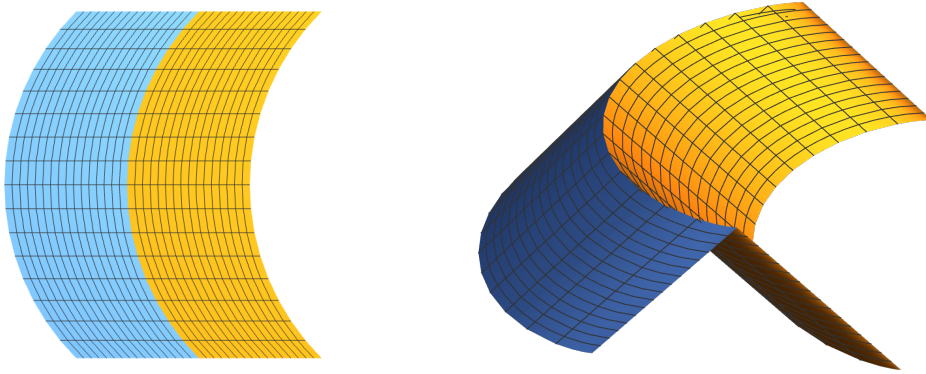


Figure 4: Example of circular arc fold line and folded crease obtained with the geometric approach.

consider the special case of a fold line shaped as a circle arc, set  $\beta(0) = \beta_0 = \pi/2$  (so that  $\beta' < 0$  in a neighborhood of  $s = 0$  and the fold line is symmetric with respect to the normal  $\bar{\mathbf{n}}(0)$ , which leads to a symmetric ridge with respect to the plane generated by  $\mathbf{n}(0)$  and  $\mathbf{b}(0)$ ), and we impose a folding angle  $\theta = \pi/2$  at  $s = 0$  (hence  $\alpha_0 = \pi/4$ ). By integrating (14) in  $(0, s)$  we obtain

$$\sin \alpha(s) = \sin \alpha_0 \frac{1}{\sin \beta(s)} \quad (\text{for } \beta_0 = \frac{\pi}{2}) \quad (15)$$

where  $\beta(s) = \pi/2 - s/R$ , and which admits solution with real  $\alpha(s)$  for any  $\alpha_0 \in (-\pi/2, \pi/2)$  as long as  $\sin \beta(s) \geq |\sin \alpha_0|$ . At  $s = s^*$  where equality holds,  $\alpha(s^*) = \pm\pi/2$  and the folding angle of the ridge either vanishes or is equal to  $2\pi$ . We write

$$\alpha(s) = \arcsin \left( \frac{\sin \alpha_0}{\sin \beta(s)} \right), \quad s \in (0, s^*)$$

and the solution above cannot be continued past  $s = s^*$  without violating non-interpenetration of the two pleats joined by the ridge. For the case  $\beta_0 = \pi/2$ , this occurs with  $\beta(s^*) = |\alpha_0|$ . **Figure 4** shows a fold line  $\bar{\gamma}$  shaped as a circular sector (arc of circle) of radius  $R$ . If  $\alpha_0$  has to be varied in the interval  $(0, \pi/4)$ , so that the mechanism at  $s = 0$  works as a hinge with folding angle  $\theta$  closing from  $\pi$  (flat) to  $\pi/2$  (in which case the two sides of the ridge are ‘orthogonal’ at  $s = 0$ ), then the maximal length of the fold-line is  $s^* = R\pi/4$  corresponding to a circular sector with opening angle  $\pi/4$  (or  $\pi/2$  for its symmetric version).

In practice, the geometric construction described above can be realized in the folding of a sheet if the isometry is rigidly enforced (i.e., if the sheet is unstretchable), and if the direction of the rulings can be prescribed a-priori. This second condition can be guaranteed if the bending energy of the sheet is anisotropic, so that the sheet is inflexible in one direction (the one of the rulings (3)) and flexible in the perpendicular one with either zero or finite bending modulus  $B \geq 0$ . This can be obtained, for example, with corrugated cardboard (**Fig. 3**), with sheets containing embedded stiff and aligned fibers or, to some extent, with sheets made of inflated parallel and unstretchable tubes (see Gao et al. (2020)).

## 2.2. Mechanical modeling

We consider two mechanical models: 1) 2D shell model; 2) 3D solid mechanics. The two models share the same geometric footprint, that is a flat rectangular surface  $\mathcal{S} = L \times W$ , with

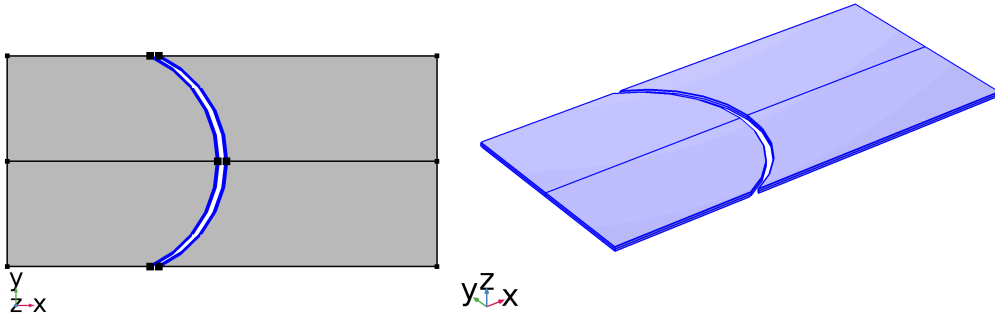


Figure 5: Geometries with two folds. Left: 2D geometry with two separate folds; the mechanical coupling is obtained by kinematical constraints on the two adjacent fold-lines (blue). Right: 3D geometry extruded from the 2D one. The mechanical coupling is obtained by the same kinematical constraints on the fold-lines used for the 2D case.

the length  $L$  and the width  $W$  parallel to the  $X$  and  $Y$  directions, respectively. The 2D region  $\mathcal{S}$  is first split into pleats by fold lines (one fold is considered in this section, two and three in the following) and then extruded along the  $Z$  direction to a 3D region of thickness  $H$  defined by  $\mathcal{V} = \mathcal{S} \times (-H/2, +H/2)$ . This 3D region  $\mathcal{V}$  represents the reference configuration of both the 3D solid and the shell-like solid; see Sections 5.1.1 and 5.1.2 for a brief summary of the theory, and Section 5.2 for the details about the geometries.

Mechanical coupling between folds is enforced through kinematic constraints. Adjacent folds are constrained to exhibit identical displacements along the fold line joining them. To enforce this constraint numerically, we observe that each physical fold line is a boundary curve for two adjacent folds, which we conventionally call the left and right folds and fold lines. Denoting the displacements of the left and right folds as  $\mathbf{u}_L$  and  $\mathbf{u}_R$ , respectively, we impose the constraint  $\mathbf{u}_R = \mathbf{u}_L$  on the right fold line; reaction forces are then applied to the left fold line to maintain this coupling.

It is worth mentioning that a key characteristic of the constraint is that it solely restricts relative translational motion between the two folds, allowing for independent rotational movement. This is because the shell model’s rotational state variables are unconstrained, and controlling linear displacement along a line in the solid model does not restrict relative rotations. Figure 5 shows the case with two folds; on the left we have the 2D geometry, with fold lines highlighted in blue, and on the right the 3D one.

The next two subsections provide detailed insight into the specific problems we addressed to compare the two modeling approaches. To assess the effectiveness of the models, we conducted tests on various geometries featuring two folds and a circular fold line with varying curvature radii,  $R_o$ . We always use the same flat region  $\mathcal{S} = L \times W$ , with  $L = 2W$ , and thickness  $H = L/100$ , using a different radius of curvature of the circular fold line:  $R_o = 0.6W, \dots, 1.1W$ .

The specific test geometry considered in these subsections allows us to address the origin of the geometric ‘tapering’ predicted by both mechanics models and observed experimentally in synthetic hygromorphic structures, see **Figure 7**. The prescribed (constant) target curvature is achieved at the edges of the rectangular cross section farthest away from the fold line, see right panel of Fig. 7. Moving towards the fold line, the observed curvature decreases to a reduced value, due to the interference of the fold line, which favors different (nonconstant) values of curvature, as shown by the geometric approach in Section 2.1. The existence of fold lines that do not interfere with the prescribed target curvature is further investigated in Section 3.

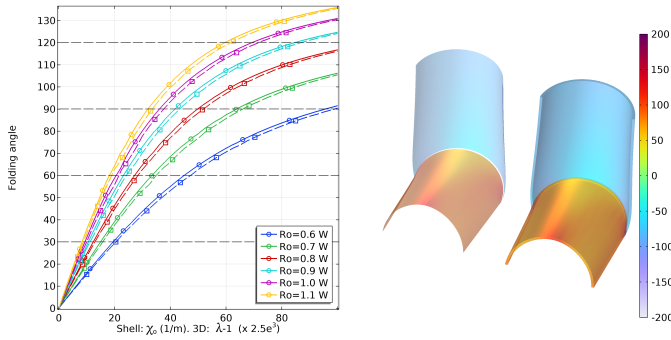


Figure 6: Comparison of shell model with 3D solid model. Left: Folding angle  $\theta_{12}$  versus the target curvature  $\chi_o$  for the shell model (solid, circle), and versus the target stretch  $\lambda_{||} - 1$  for the 3D model (dashed, square). To align the x-coordinates we rescale the stretch by  $2.5 \cdot 10^3 (\lambda_{||} - 1)$ . Center: two configurations for  $R_o = 0.7W$ , at  $\chi_o = 100$  1/m and  $\lambda_{||} - 1 = 0.04$ , side by side (left=shell; right=3D). Right: the previous two configurations superimposed each other.

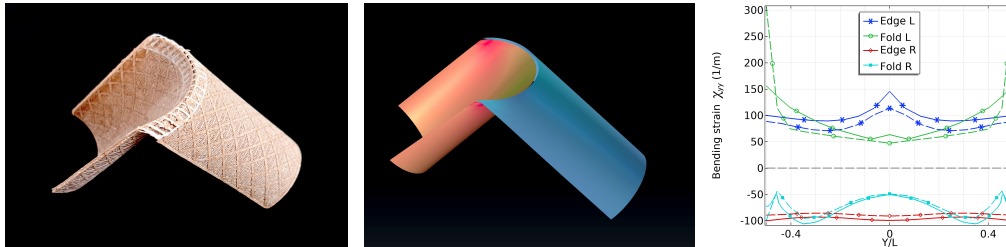


Figure 7: Left. The hygromorph, courtesy of T. Cheng and Y. Tahouni. Center. Result from shell model;  $R_o = 0.6W$ ,  $\chi_o = 100$  1/m. Right. Bending strain  $\chi_{yy}$  versus  $Y/W$  along four lines; left (red fold) and right (blue fold) refers to the image at center. The solid lines correspond to the results obtained from the shell model, whereas the dashed lines correspond to the results from the 3D solid model.

### 2.2.1. Approach by active shell models: actuation by target curvature

We solve the weak equation (31), using as only input the target curvature  $\chi_o$ ; the deformed configurations are obtained by assigning the target curvature  $\chi_o$  with only one non trivial component; we have:

$$\chi_o = \begin{bmatrix} 0 & 0 \\ 0 & \chi_{o,yy} \end{bmatrix}; \quad \text{thus, } \chi_e = \begin{bmatrix} \chi_{xx} & \chi_{xy} \\ \chi_{xy} & \chi_{yy} - \chi_{o,yy} \end{bmatrix}. \quad (16)$$

The bending term in the shell energy (30) is zero when  $\chi_e = 0$ , that is when the actual curvature is equal to the target one; in general, this equality cannot be realized, and the minimum of the energy is obtained with all the three terms different from zero; in our models, the bending energy is the leading one.

In particular, for each shell, we solve for the configurations  $C_i$  corresponding to a sequence of  $n$  pairs  $K_i = (\chi_{oi}, -\chi_{oi})$ , where  $\chi_{oi}$  are the target curvatures assigned to the first fold and  $-\chi_{oi}$  the ones of the second fold;  $\chi_{oi}$  ranges in  $(0, \chi_m)$  (1/m).

### 2.2.2. Approach by 3D active elasticity models: actuation by target metric

We solve the weak equation (21), using as only input a target strain. The deformed configurations are obtained by assigning a target strain  $\mathbf{E}_o$  parametrized by the stretch  $\lambda_{||}$ , see (19). In particular, each of the two folds is split by a horizontal plane of symmetry in the bottom and top



halves; we set  $\lambda_{\parallel} = 1$  in the bottom-left and top-right regions, and we solve for the configurations  $\mathcal{C}_i$  corresponding to a sequence of  $n$  target stretches  $\lambda_i = \lambda_{\parallel i}$ , with  $\lambda_1 = 1$  and  $\lambda_n = \lambda_{max} > 1$ ; we use a minimal set of kinematical constraints that rule out rigid motions without inducing reactive forces.

### 3. Role of geometry of a single fold-line: circular arcs vs trigonometric functions

Following the modeling approach described in Sec. 2.2.1, we compare the behavior of flat rectangular shells  $\mathcal{S} = L \times W$  split in two folds by different fold lines: 1) circular arc; 2) trigonometric function. The geometries are described in Sec. 5.2. The shells are not loaded, and have compatible constraints, that is the deformations they exhibit do not generate reaction forces; the only input is the target curvature  $\chi_o$ , see (16).

For both shells, we solve for the configurations  $\mathcal{C}_i$  corresponding to a sequence of  $n$  pairs  $X_{oi} = (\chi_{oi}, -\chi_{oi})$ , where  $\chi_{oi}$  are the target curvatures assigned to the first fold and  $-\chi_{oi}$  the ones of the second fold;  $\chi_{oi}$  ranges in  $(0, \chi_m)$  (1/m).

We discuss the results showing: 1) the folding angle  $\theta_{12} = 2\alpha_{12}$  between the first and the second fold. 2) the actual curvature  $\chi_{yy}$  of the deformed configuration  $\mathcal{C}$  evaluated along the center line; 3) the elastic energy density (energy per unit area).

The main result is that for the circular fold line, any value of the target curvature  $\chi_o$  is incompatible and increases the energy of the shell; see Fig. 8. However, this energy is mostly due to bending ( $W_b$ ), while the membrane contribution ( $W_s$ ) is comparatively smaller. As shown in the inset, this is particularly true in the regime of moderate folding angles, the ones smaller than  $90^\circ$  where the geometric construction of Section 2.1 applies. For completeness, we also show the shear contribution  $W_s$ . Conversely, for the trigonometric fold line there exists a value of the target curvature, and hence of the folding angle, that yields a compatible folding, where also the bending energy vanishes. For this geometry, this special curvature is  $\chi_o = 100$  1/m and the corresponding folding angle is  $110^\circ$ , see Fig. 9. To achieve this folding angle, an energy barrier with significant contributions from both membrane and bending energies needs to be overcome.

We note that using the trigonometric function, it is possible to design a fold line that achieves a compatible configuration at a given value of the target curvature  $\chi_o$ . In Figure 10 we show the results corresponding to three different fold line parametrized by  $\vartheta_o = 75^\circ, 60^\circ, 45^\circ$ , that at  $\chi_o = 100$  1/m, yields the folding angles  $\theta_{12} = 30^\circ, 60^\circ, 90^\circ$ , respectively. For all three cases, the energy is not monotone with  $\chi_o$ ; after increasing, it goes back to zero as consequence of the compatibility at  $\chi_o = 100$  1/m.

### 4. Interaction between folds: synchronous vs sequential folding in an array of 4 identical circular folds

We consider a flat rectangular shell  $\mathcal{S} = L \times W$  split in four folds by three circular fold-lines. We look for the configuration associated to given values of the target curvatures  $\chi_{oj}$  in each fold  $j = 1, \dots, 4$ . In particular, we assign a sequence of  $n$  quadruplets  $X_{oi} = (\chi_{o1}, \dots, \chi_{o4})_i$ , with  $i = 1, \dots, n$  and  $\chi_{oi}$  ranging in  $(0, \pm\chi_m)$  (1/m), and we solve for the corresponding configuration  $\mathcal{C}_i$ ; we denote with  $\theta_{hk} = 2\alpha_{hk}$  the folding angle between fold  $h$  and  $k$ . Two different sequences are used:

- Sync (Synchronized):  $X_{oi} = (-\chi_{o1}, \chi_{o1}, -\chi_{o1}, \chi_{o1})_i$ . The alternating sign  $\pm$  of the target curvatures in the adjacent folds yields an almost compatible deformation; the change of configuration is smooth, and associated to a low increase of elastic energy.

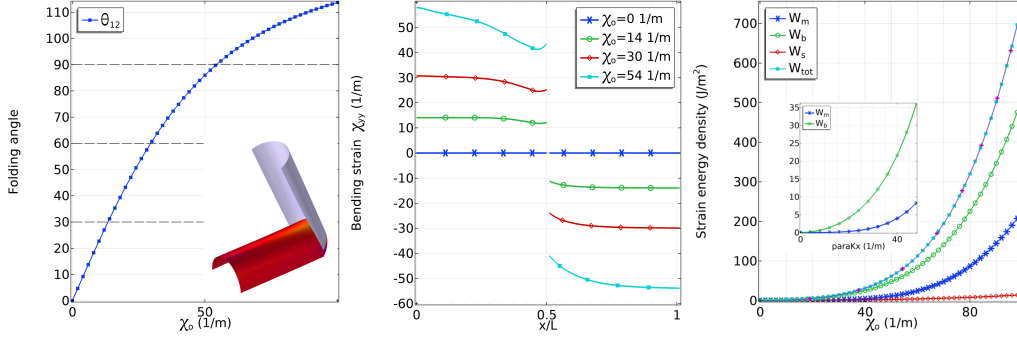


Figure 8: Result for circular fold-line. Left: Folding angle  $\theta_{12}$  between the two folds; the inset shows the configuration at  $\chi_o = 100$  1/m. Center: Current bending strain  $\chi_{yy}$  versus  $X/L$  along the center line of the shell for three different values of the target curvature  $\chi_o$  evaluated at the folding angles  $\theta_{12} = 30^\circ, 60^\circ, 90^\circ$ . It might be noticed that current  $\chi_{yy}$  differs from the target curvature  $\chi_o$  as consequence of the incompatibility of the curvature assigned to the two folds. The difference between  $\chi_{yy}$  and  $\chi_o$  increases with the folding angle. Right: Elastic energies versus target curvature  $\chi_o$ ; energies increases with  $\chi_o$ , a consequence of the aforementioned incompatibility of  $\chi_o$ .

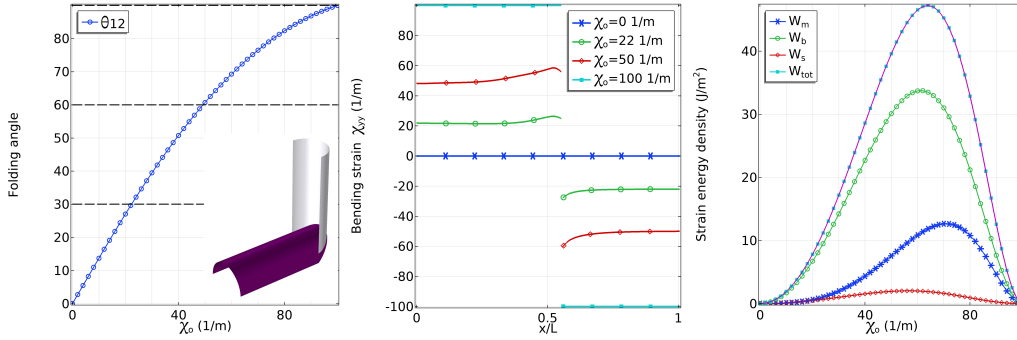


Figure 9: Result for trigonometric fold-line. Left: Folding angle  $\theta_{12}$  between the two folds; the inset shows the configuration at  $\chi_o = 100$  1/m. Center: Current bending strain  $\chi_{yy}$  versus  $X/L$  along the center line of the shell for three different values of the target curvature  $\chi_o$  evaluated at the folding angles  $\theta_{12} = 30^\circ, 60^\circ, 90^\circ$ . It might be noticed that current  $\chi_{yy}$  differs from the target curvature  $\chi_o$  as consequence of the incompatibility of the curvature assigned to the two folds, but contrary to the previous case with circular fold-line, at  $\theta_{12} = 90^\circ$  we have  $\chi_{yy} = \chi_o$ , that is  $\chi_o = 100$  1/m is a compatible target curvature. Right: Elastic energies versus target curvature  $\chi_o$ ; it might be noticed that energies are not monotone with  $\chi_o$ ; after increasing, they go back to zero as consequence of compatibility a target curvature  $\chi_o = 100$  1/m.

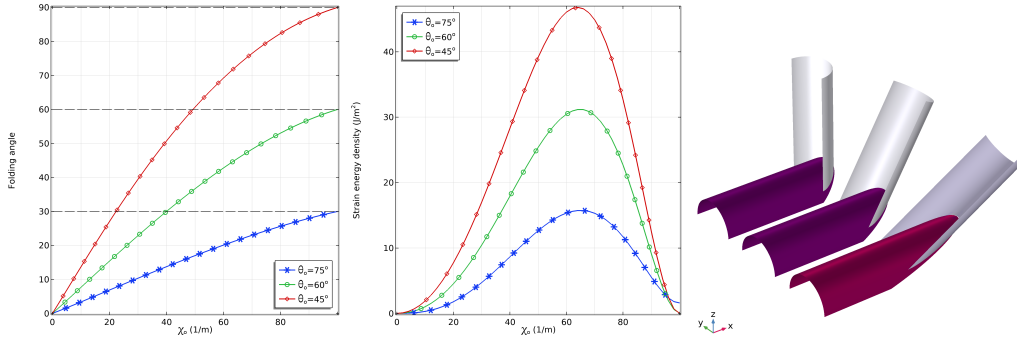


Figure 10: Result for trigonometric fold-line with three different  $\vartheta_o$ . Left: Folding angle  $\theta_{12}$  between the two folds; each fold-line has been designed to have a compatible configuration at  $\chi_o = 100$  1/m, and with folding angles  $\theta_{12} = 30^\circ, 60^\circ, 90^\circ$ . Center: Elastic energies versus target curvature  $\chi_o$ ; it might be noticed that energies are not monotone with  $\chi_o$ ; after increasing, they go back to zero as consequence of compatibility a target curvature  $\chi_o = 100$  1/m. Right: the three final configurations at  $\chi_o = 100$  1/m.

- Seq (Sequential): the whole sequence  $X_{oi}$  is split into three sub sequences.

$$\begin{aligned}
 X_{oi} &= (-\chi_{01}, \chi_{01}, \chi_{01}, \chi_{01})_i, \quad \text{with } \chi_{01} = 0, \dots, \chi_m, \quad i = 1, \dots, n_1, \\
 X_{oi} &= (-\chi_m, \chi_m, \chi_{03}, -\chi_{03})_i, \quad \text{with } \chi_{03} = \chi_m, \dots, -\chi_m, \quad i = n_1 + 1, \dots, n_2, \\
 X_{oi} &= (-\chi_m, \chi_m, -\chi_m, \chi_{04})_i, \quad \text{with } \chi_{04} = -\chi_m, \dots, \chi_m, \quad i = n_2 + 1, \dots, n_3,
 \end{aligned} \tag{17}$$

The first sequence changes only the angle  $\theta_{12}$  between the first fold and the next three. The second one maintains  $\theta_{12}$  constant, and only changes  $\theta_{23}$ ; the final sequence maintains both  $\theta_{12}$  and  $\theta_{23}$  constant, and changes  $\theta_{34}$ . The change of configuration might exhibit jumps, and elastic energy is not monotone with the solution number  $i$ .

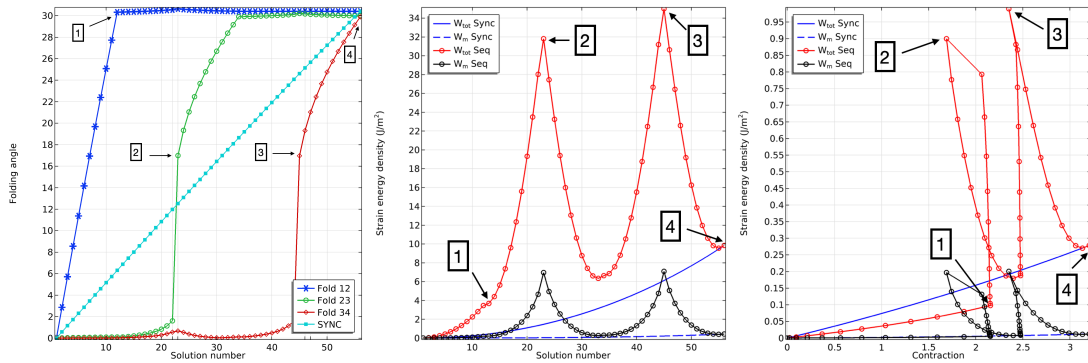


Figure 11: Elastic energy versus solution number for the synchronized and the sequential folding. The four numbered points correspond to the configurations in Fig. 12.

## 5. Interaction between folds: fold pairs of circular and trigonometric arcs with different radii or heights

Following the modeling approach described in Sec. 2.2.1, we compare the behavior of flat rectangular shells  $\mathcal{S} = L \times W$  split in three folds by different pair of fold-lines: 1) two circular

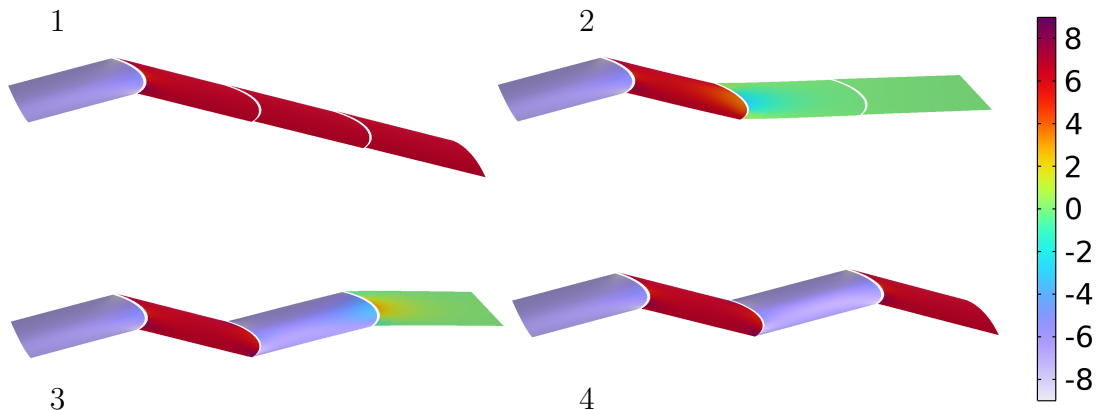


Figure 12: Four different configurations of the shell made of four folds, undergoing a sequential folding; circular fold-lines. Color legend shows the bending strain  $\chi_{yy}$  in the transversal direction (1/m).

arcs, with different curvature radii  $R_o$ ; 2) two trigonometric function, with different amplitude. The geometries are described in Sec. 5.2. The shells are not loaded, and have compatible constraints, that is the deformations they exhibit do not generate reaction forces; the only input is the target curvature  $\chi_o$ , see (16).

For both shells, we solve for the configurations  $\mathcal{C}_i$  corresponding to a sequence of  $n$  triplets  $X_{oi} = (\chi_{oi}, -\chi_{oi}, \chi_{oi})$ , where  $\chi_{oi}$  are the target curvatures assigned to the first and third fold and  $-\chi_{oi}$  the ones of the middle fold;  $\chi_{oi}$  ranges in  $(0, \chi_m)$  (1/m).

We discuss the results showing: 1) the folding angles  $\theta_{12} = 2\alpha_{12}$  between the first and the second fold, and  $\theta_{23} = 2\alpha_{23}$  between the second and the third fold,

2) the actual curvature  $\chi_{yy}$  of the deformed configuration  $\mathcal{C}$  evaluated along the center line; 3) the elastic energy density (energy per unit area).

The main result is that both geometries exhibit two different folding angles, that is  $\theta_{12} \neq \theta_{23}$ . Moreover, as already observed, for the circular fold line, any value of the target curvature  $\chi_o$  is incompatible and increases the energy of the shell; see Fig. 13. Conversely, for the trigonometric fold-line there exists a value of the target curvature that yields a compatible folding: for this geometry it is  $\chi_o = 100$  1/m, see Fig. 14.

## 5.1. Mechanics modeling

### 5.1.1. The 3D model

The reference configuration of the 3D solid is described by  $\mathbf{X} = (X, Y, Z)$ , where  $(X, Y, Z)$  are the material coordinates of  $\mathcal{V}$ . The current positions  $x = (x, y, z)$  of material points  $X$  are given by  $x = X + \mathbf{u}(X)$ , with  $\mathbf{u}$  the displacement. The strain  $\mathbf{E}$  and stress  $\mathbf{S}$  are defined by

$$\mathbf{E} = \frac{1}{2} (\nabla \mathbf{u} + \nabla \mathbf{u}^T + \nabla \mathbf{u}^T \nabla \mathbf{u}), \quad \mathbf{S} = \mathbb{C} \mathbf{E}_e, \quad \text{and } \mathbf{E}_e = \mathbf{E} - \mathbf{E}_o, \quad (18)$$

where  $\mathbb{C}$  is the elastic tensor corresponding to an isotropic material, and  $\mathbf{E}_e$  is the elastic strain. The target strain  $\mathbf{E}_o$  is defined by

$$\mathbf{E}_o = \lambda_{\parallel} \mathbf{e}_2 \otimes \mathbf{e}_2 + \lambda_{\perp} (\mathbf{e}_1 \otimes \mathbf{e}_1 + \mathbf{e}_3 \otimes \mathbf{e}_3), \quad \text{with } \lambda_{\parallel} = 1 + \varepsilon, \lambda_{\perp} = 1. \quad (19)$$

The target strain  $\mathbf{E}_o$  yields a distortion along the  $Y$  direction which induces a bending in the plane  $(Y, Z)$ . The elastic energy  $\Psi$  is given by

$$\Psi = \frac{1}{2} \mathbb{C} \mathbf{E}_e \cdot \mathbf{E}_e \quad (20)$$

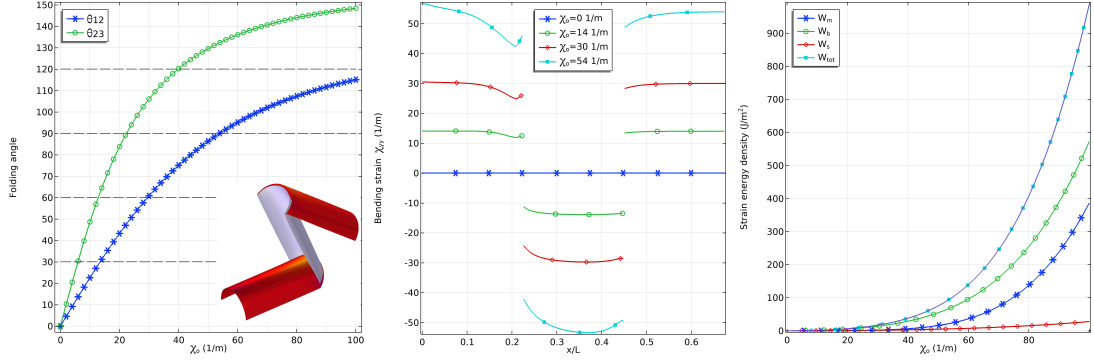


Figure 13: Result for two different circular fold-lines. Left: Folding angle  $\theta_{12}$  and  $\theta_{23}$  between the two pairs of adjacent folds; we note that for any  $\chi_o$  there correspond different folding angles. The inset shows the configuration at  $\chi_o = 100$  1/m. Center: Current bending strain  $\chi_{yy}$  versus  $X/L$  along the center line of the shell for three different values of the target curvature  $\chi_o$  evaluated at the folding angles  $\theta_{12} = 30^\circ, 60^\circ, 90^\circ$ . It might be noticed that current  $\chi_{yy}$  differs from the target curvature  $\chi_o$  as consequence of the incompatibility of the curvature assigned to the three folds. The difference between  $\chi_{yy}$  and  $\chi_o$  increases with the folding angle. Right: Elastic energies versus target curvature  $\chi_o$ ; it might be noticed that energies increases with  $\chi_o$ , a consequence of the aforementioned incompatibility of  $\chi_o$ .

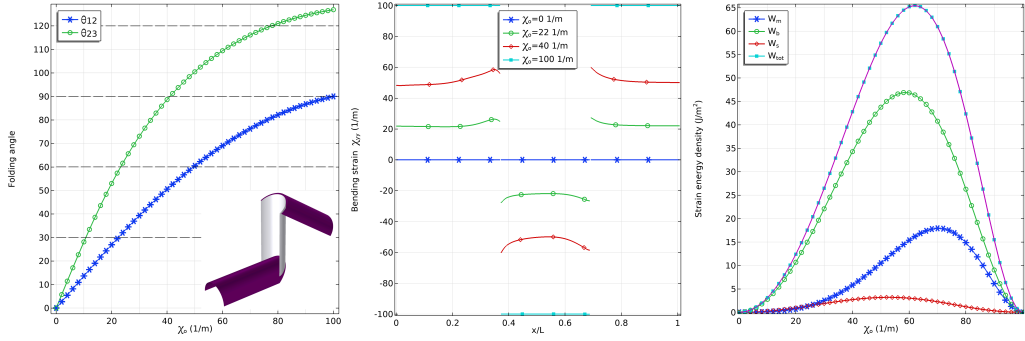


Figure 14: Result for two different trigonometric fold-lines. Left: Folding angle  $\theta_{12}$  and  $\theta_{23}$  between the two pair of adjacent folds; we note that for any  $\chi_o$  there correspond different folding angles. The inset shows the configuration at  $\chi_o = 100$  1/m. Center: Current bending strain  $\chi_{yy}$  versus  $X/L$  along the center line of the shell for three different values of the target curvature  $\chi_o$  evaluated at the folding angles  $\theta_{12} = 30^\circ, 60^\circ, 90^\circ$ . The current  $\chi_{yy}$  differs from the target curvature  $\chi_o$  as consequence of the incompatibility of the curvature assigned to the three folds, but contrary to the previous case with circular fold-lines, at  $\theta_{12} = 90^\circ$  we have  $\chi_{yy} = \chi_o$ , that is  $\chi_o = 100$  1/m is a compatible target curvature for both folds. Right: Elastic energies versus target curvature  $\chi_o$ ; the energies are not monotone with  $\chi_o$ , and after increasing, they go back to zero as consequence of compatibility at  $\chi_o = 100$  1/m.

Finally, assuming no loads, global energy minimization yields to the following weak equation:

$$\int_{\mathcal{V}} \mathbf{S} \cdot \tilde{\mathbf{E}}_e dV = 0, \quad \forall \tilde{\mathbf{u}}. \quad (21)$$

We solve (21) using as input a sequence of target stretches  $\lambda_{\parallel} = 1, \dots, \lambda_{max}$ , with a minimal set of kinematical constraints that rule out rigid motions without inducing reactive forces.

### 5.1.2. The Shell model

The reference configuration of the shell-like region is given by

$$\mathbb{R}^3 \ni \mathbf{X} = \mathbf{X}(\xi_1, \xi_2, \xi_3) = \mathbf{s}(\xi_1, \xi_2) + \xi_3 \mathbf{N}(\xi_1, \xi_2). \quad (22)$$

where  $\mathbf{s} : \mathbb{R}^2 \rightarrow \mathbb{R}^3$  is the reference shell surface,  $\mathbf{N}$  the shell normal, and  $\xi_i$  are the local coordinates on  $\mathcal{S}$ . The coordinate  $\xi_3$  in the normal direction ranges in  $(-H/2, +H/2)$ . The state variables of the shell model are the displacement  $\mathbf{u}$ , yielding the current position of the reference shell surface  $\mathcal{S}$ , and the vector  $\mathbf{a}$  that gives the current normal  $\mathbf{n} = \mathbf{N} + \mathbf{a}$ . The current configuration of the 3D shell-like region is given by

$$\mathbf{x} = \mathbf{x}(\xi_1, \xi_2, \xi_3) = \mathbf{s}(\xi_1, \xi_2) + \mathbf{u}(\xi_1, \xi_2) + \xi_3 \mathbf{n}(\xi_1, \xi_2). \quad (23)$$

Let the indices  $\alpha$  and  $\beta$  range in 1, 2. The in plane Green-Lagrange strains are measured by

$$\epsilon_{\alpha\beta} = \frac{1}{2} \left( \frac{\partial \mathbf{x}}{\partial \xi_\alpha} \cdot \frac{\partial \mathbf{x}}{\partial \xi_\beta} - \frac{\partial \mathbf{X}}{\partial \xi_\alpha} \cdot \frac{\partial \mathbf{X}}{\partial \xi_\beta} \right) = \gamma_{\alpha\beta} + \xi_3 \chi_{\alpha\beta} + O(\xi_3^2) \doteq \gamma_{\alpha\beta} + \xi_3 \chi_{\alpha\beta}. \quad (24)$$

The transverse shear is given by

$$\epsilon_{3\alpha} = \epsilon_{\alpha 3} = \frac{1}{2} \left( \frac{\partial \mathbf{x}}{\partial \xi_\alpha} \cdot \mathbf{n} - \frac{\partial \mathbf{X}}{\partial \xi_\alpha} \cdot \mathbf{N} \right) = \zeta_\alpha + O(\xi_3) \doteq \zeta_\alpha. \quad (25)$$

Note that the contributions of order  $O(\xi_3^2)$  from  $\epsilon_{\alpha\beta}$ , and order  $O(\xi_3)$  from  $\epsilon_{3\alpha}$  have been considered negligible, as well as  $\epsilon_{33}$ . The remaining contributions are called *membrane strain*  $\gamma_{\alpha\beta}$ , *bending*  $\chi_{\alpha\beta}$ , and *shear*  $\zeta_\alpha$ . The membrane stress  $\sigma_m$ , the bending stress  $\sigma_b$  and the shear stress  $\sigma_s$  are given by

$$\sigma_m = \mathbf{D} (\gamma - \gamma_o), \quad \sigma_b = \frac{H}{2} \mathbf{D} (\chi - \chi_o), \quad \sigma_s = \frac{5}{6} 2G (\zeta - \zeta_o), \quad (26)$$

where  $\mathbf{D}$  is the 2D plane stress constitutive matrix corresponding to the 3D elastic tensor  $\mathbb{C}$ ,  $G$  the transverse shear moduli, and  $\gamma_o, \chi_o, \zeta_o$  are the target or target strains. The current stress  $\sigma$  in the 3D shell-like region is recovered by the formula  $\sigma = \sigma_m + z \sigma_b$ , with  $z$  is a non dimensional coordinate ranging from  $-1$  (bottom surface) to  $1$  (top surface). The shell membrane-force  $\mathbf{N}_m$ , bending moment  $\mathbf{M}_b$ , and shear force  $\mathbf{Q}_s$  are computed from the stresses as follows

$$\mathbf{N}_m = H \sigma_m, \quad \mathbf{M}_b = \frac{H^2}{6} \sigma_b, \quad \mathbf{Q}_s = H \sigma_s. \quad (27)$$

The previous constitutive relations might be rewritten in matrix form as:

$$\begin{bmatrix} \mathbf{N}_m \\ \mathbf{M}_b \\ \mathbf{Q}_s \end{bmatrix} = \begin{bmatrix} \mathbf{D}_A & \mathbf{D}_B & 0 \\ \mathbf{D}_B & \mathbf{D}_D & 0 \\ 0 & 0 & \mathbf{D}_{AS} \end{bmatrix} \begin{bmatrix} \gamma_e \\ \chi_e \\ \zeta_e \end{bmatrix}, \quad \text{with } \gamma_e = \gamma - \gamma_o, \chi_e = \chi - \chi_o, \zeta_e = \zeta - \zeta_o. \quad (28)$$

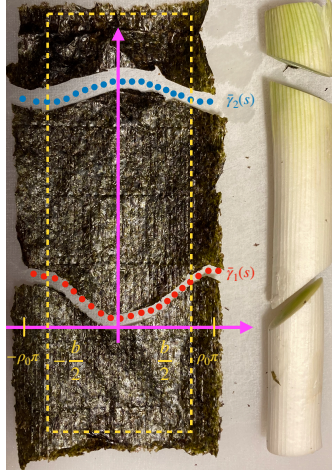


Figure 15: Illustration of the unfolding of an oblique section of a right cylinder onto a plane, leading to trigonometric fold lines.

The stiffness matrices in (28) have following IS units:

$$[\mathbf{D}_A] = \text{N/m}, \quad [\mathbf{D}_B] = \text{N}, \quad [\mathbf{D}_D] = \text{Nm}, \quad [\mathbf{D}_{AS}] = \text{N/m}. \quad (29)$$

The elastic energy  $\psi_{ela}$  can be represented as the sum of the membrane  $\psi_m$ , the bending  $\psi_b$ , and the shear energy  $\psi_s$  as follows:

$$\begin{aligned} \psi_{ela} &= \psi_m + \psi_b + \psi_s \\ &= \frac{1}{2} (\mathbf{D}_A \gamma_e + \mathbf{D}_B \chi_e) \cdot \gamma_e + \frac{1}{2} (\mathbf{D}_B \gamma_e + \mathbf{D}_D \chi_e) \cdot \chi_e + \frac{1}{2} \mathbf{D}_{AS} \zeta_e \cdot \zeta_e \\ &= \frac{1}{2} \mathbf{N}_m \cdot \gamma_e + \frac{1}{2} \mathbf{M}_b \cdot \chi_e + \frac{1}{2} \mathbf{Q}_s \cdot \zeta_e. \end{aligned} \quad (30)$$

Finally, assuming no loads, global energy minimization yields the following weak equations:

$$\int_S \left( \mathbf{N}_m \cdot \tilde{\gamma} + \mathbf{M}_b \cdot \tilde{\chi} + \mathbf{Q}_s \cdot \tilde{\zeta} \right) dA = 0, \quad \forall \tilde{\gamma}, \tilde{\chi}, \tilde{\zeta}. \quad (31)$$

### 5.2. Geometries

We list the shell geometries used to implement and solve our problems. The footprint of each geometry is defined by a rectangle  $L \times W$ ; the shell thickness is  $H = L_o/100$ . The width  $W$  is defined by:  $W = \pi \rho_o$  for the circular fold-line;  $W = 2 \varphi \rho_o$  for the trigonometric fold line. Finally,  $\rho_o = 1$ , and  $h_o = 2 \rho_o \tan(\vartheta_o)$ ,  $\vartheta_o = 40^\circ$ . The trigonometric fold line is obtained from the oblique section of a right cylinder with a plane (radius  $\rho_o$ , angle  $\vartheta_o$ ), by unfolding the cylinder onto a plane, see Fig. 15. For each fold line  $i$ , we have:  $c_i$  = base point;  $X_i$  and  $Y_i$  parametric curve;  $s \in (-\varphi, \varphi)$  abscissa of the curve.

*1 Fold:*  $L = L_o = 2W$  or  $3W$ ;  $R_o = L_o/4$ .

- Circular arc;  $\varphi = \arcsin(2/3)$ .

$$c_1 = (L/4, 0), \quad \begin{cases} X_1 = R_o \sin(s + \pi/2) \\ Y_1 = R_o \cos(s + \pi/2) \end{cases} \quad (32)$$

- Trigonometric function;  $\varphi = \pi/2$ .

$$c_1 = (L/2 - h_o/4 \sin(\varphi), 0), \quad \begin{cases} X_1 = h_o/2 \sin(s + \pi/2) \\ Y_1 = \rho_o s \end{cases} \quad (33)$$

2 Folds:  $L = 3 L_o/2$ , and  $L_o = 3 W$ ,  $R_o = L_o/4$ .

- Circular arc, different folds;  $\varphi_1 = \arcsin(2/3)$ ,  $\varphi_2 = \arcsin(1/3)$ ,

$$c_1 = (L_o/2, 0), \quad \begin{cases} X_1 = R_o \sin(s + \pi/2) \\ Y_1 = R_o \cos(s + \pi/2) \end{cases}, \quad c_2 = (L_o, 0), \quad \begin{cases} X_2 = 2 R_o \sin(s + \pi/2) \\ Y_2 = 2 R_o \cos(s + \pi/2) \end{cases}, \quad (34)$$

- Trigonometric function, different folds;  $\varphi = \arcsin(2/3)$ .

$$c_1 = (L_o/2 - h_o/4 \sin(\phi), 0), \quad \begin{cases} X_1 = h_o/2 \sin(s + \pi/2) \\ Y_1 = \rho_o s \end{cases}, \quad (35)$$

$$c_2 = (L_o - h_o/8 \sin(\phi), 0), \quad \begin{cases} X_2 = h_o/4 \sin(s + \pi/2) \\ Y_2 = \rho_o s \end{cases},$$

3 Folds:  $L = 2 L_o$ ,  $L_o = 2.82 W$ , and  $W = L_o/2 \sin(\pi/4)$ .

- Circular arc, same folds;  $\varphi = \pi/4$ ,

$$c_1 = (L_o/2, 0), \quad c_2 = (L_o, 0), \quad c_3 = (3 L_o/2, 0), \quad \begin{cases} X_i = L_o/4 \sin(s + \pi/2) \\ Y_i = L_o/4 \cos(s + \pi/2) \end{cases}, \quad (36)$$

## Acknowledgments

We gratefully acknowledge the support by the European Research Council through ERC PoC Grant Stripe-o-Morph (GA 101069436), by the EU H2020 program through I-Seed (GA 101017940) and Storm-Bots (GA 956150) projects, by the EU Horizon Europe program through MapWorms (GA 101046846) project by the Italian Ministry of Research through the projects Response (PRIN 2020), Abyss (PRIN 2022), and Innovative mathematical models for soft matter and hierarchical materials (PRIN 2022, PNRR F53D2300283 0006). The authors ADS and LT are members of the INdAM GNFM research group. ADS acknowledges useful discussions with Richard James, to whom this paper is dedicated, and with members of the research group Adaptive Beauty (J. Bico, B. Roman, T. Gao, N. Vani, T. Cheng, Y. Tahouni).

## References

- Alese, L., 2022. Propagation of curved folding: the folded annulus with multiple creases exists. *Beiträge zur Algebra und Geometrie/Contributions to Algebra and Geometry* 63, 19–43.
- do Carmo, M.P., 1976. *Differential Geometry of curves and surfaces*. Paperback.
- Demaine, E.D., Demaine, M.L., Huffman, D.A., Koschitz, D., Tachi, T., 2018. Conic crease patterns with reflecting rule lines. arXiv preprint arXiv:1812.01167 In *Origami*<sup>7</sup>, Vol. 2. Tarquin, 574–590.



- Feng, F., Dradrach, K., Zmyślony, M., Barnes, M., Biggins, J.S., 2024. Geometry, mechanics and actuation of intrinsically curved folds. *Soft Matter* 20, 2132–2140.
- Fuchs, D., Tabachnikov, S., 2006. *Mathematical Omnibus: 30 lectures on classic mathematics*. American Mathematical Society.
- Gao, T., Siéfert, E., DeSimone, A., Roman, B., 2020. Shape programming by modulating actuation over hierarchical length scales. *Advanced Materials* 32, 2004515.
- Jiang, C., Mundilova, K., Rist, F., Wallner, J., Pottmann, H., 2019. Curve-pleated structures. *ACM Transactions on Graphics (TOG)* 38, 1–13.
- Liu, H., James, R.D., 2024. Design of origami structures with curved tiles between the creases. *Journal of the Mechanics and Physics of Solids* 185, 105559.
- Tachi, T., 2011. One-dof rigid foldable structures from space curves, in: *Proceedings of the IABSE-IASS Symposium*, pp. 20–23.
- Tahouni, Y., Cheng, T., Wood, D., Sachse, R., Thierer, R., Bischoff, M., Menges, A., 2020. Self-shaping curved folding: A 4d-printing method for fabrication of self-folding curved crease structures, in: *Proceedings of the 5th Annual ACM Symposium on Computational Fabrication*, pp. 1–11.